(Received 26 February 2024, Accepted 5 April 2024, Scheduled 10 April 2024)

Design of a Three-Channel Frequency Multiplexing Metasurface in Full Space

Qinxuan Ling[1,2], Jinfeng He[1,*], Honggang Hao[1], Zhonglyu Cai[1], and Min Wang[1]

[1]*School of Optoelectronic Engineering, Chongqing University of Posts and Telecommunications, Chongqing, China*
[2]*Chongqing GigaChip Technology Co.Ltd., China*

ABSTRACT: The multifunctional metasurface offers a high degree of flexibility in manipulating electromagnetic waves. However, the majority of its functions are limited to the reflection or transmission space in a single band, restricting the utilization of electromagnetic information. This paper proposes a three-channel multifunctional frequency multiplexing coding metasurface based on the Fabry-Perot cavity principle. It consists of two layers of orthogonal metal gratings and a cross-shaped, oblique open loop structure in the intermediate layer. Simulation results reveal that at an incidence of 22 GHz, the polarization conversion and focusing functions of the transmitted wave are accomplished. Similarly, at an incidence of 31 GHz, the beam deflection function of the reflected wave is observed. Furthermore, at an incidence of 32 GHz, the radar scattering cross-section reduction function of the reflected wave is achieved. In addition to achieving high efficiency, miniaturization, and compactness, the proposed metasurface effectively enhances the spatial utilization of electromagnetic information. As a result, potential applications in multifunctional integrated systems, including wireless communication, sensing technologies, and radar systems, are vast.

1. INTRODUCTION

Metasurface, a structure consisting of two-dimensional metamaterial units [1], has the benefits of a thin structure, easy fabrication, and flexible electromagnetic wave control [2, 3], attracting great interest among researchers and scholars. It is feasible to alter the amplitude, phase, and polarization of electromagnetic waves by discretizing the parameter size of the unit structure [4–6]. In 2014, coded metasurfaces were proposed by Cui's group [7], analogizing the structure of units with different phase responses to a binary code. The phase discretization of 2π can be broadened from 1-bit to multi-bits [8, 9], further simplifying the design and manufacturing of metasurface devices. Despite the limited number of encoded states, coded metasurfaces are usable to effectuate applications such as anomalous deflection [10], radar cross section (RCS) reduction [11, 12], and vortex wave generation [13, 14].

Due to the rapid advancement of integrated and miniaturized systems, 5G/6G communications, and wireless sensing technology [15, 16], there is a growing demand for multifunctional integration within a single structure [17]. Thus, multifunctional metasurfaces have been a hot research topic in both the microwave and optical fields. The array may perform various modulation functions for electromagnetic waves by designing unit structures that result in diverse flexible multiplexing, such as polarization multiplexing and frequency multiplexing [18, 19]. Traditional multifunctional unit structures can be stacked with multiple layers, but electromagnetic waves transmitted through multiple layers will generate high losses [20]. Additionally, active devices typically require external circuits [21], which can generate metasurface complexity and power consumption while achieving multifunctional electromagnetic wave control.

For multifunctional metasurfaces, Dong et al. [22] ingeniously conceived a single-layer reflective multiplexing coded metasurface that can realize frequency and polarization multiplexing. A four-band dual circular transmission metasurface with polarization conversion was proposed by Li et al. [23]. In each of the four frequency bands, this metasurface may turn line polarization waves into transmitted left-hand and right-hand circular polarization waves. Shang et al. [24] proposed a reflectance-transmission integrated metasurface. By operating at the same frequency, various focusing functionalities can be attained in both the reflection and transmission channels for different incident directions. This enables the manipulation of asymmetric characteristics of electromagnetic waves. Although metasurfaces have been proven to offer control over multiple channels and improve the utilization of electromagnetic information, the research on realizing multi-channel, multifunctional, full-space, and multiplexing metasurfaces still faces challenges.

A three-layer frequency multiplexing coded metasurface that exhibits the excellent performance of a three-channel multifunction in the entire space is presented in response to the issue of traditional metasurfaces. As a proof of concept, theoretical calculations and Computer Simulation Technology (CST) simulation analysis are used. The results indicate that under the excitation of x-polarized incident waves along the $-z$ direction, polarization conversion and focusing functions of transmitted waves can be achieved at 22 GHz. Similarly, anomalous beam deflection and RCS reduction are accomplished under the ex-

* Corresponding author: Jinfeng He (hejinfeng0502@163.com).

citation of y-polarized waves incident along the $+z$ direction at 31 GHz and x-polarized waves incident along the $-z$ direction at 32 GHz, respectively. The architecture of the paper is organized as follows.

Section 1 is the introduction, which mainly introduces the current research status of digital coding, multifunctional, and multiplexing metasurfaces, and Section 2 primarily talks about the principle of the Fabry-Perot resonant cavity used in this paper, laying a theoretical foundation for subsequent design. Section 3 is the design and result analysis of the metasurface unit structure, as well as the coding sequence scheme for its discrete phase. Section 4 presents the design, simulation, and analysis of a three-channel multifunctional metasurface. Section 5 is the conclusion, summarizing the innovation and shortcomings of this work and providing application scenarios and development directions for multifunctional multiplexing metasurfaces.

2. PRINCIPLE ANALYSIS OF FABRY-PEROT CAVITY UNIT

For structure design, a multi-degree of freedom electromagnetic response in the frequency band, polarization, and direction of incidence of electromagnetic waves needs to be exhibited by the unit. This makes it possible to control multiple types of electromagnetic waves on the metasurface array. As shown in Figure 1, the topology of the full-space unit can be regarded as a Fabry-Perot cavity based on multiple interference theory. Electromagnetic waves with different polarization components are reflected and transmitted internally, which can improve the utilization rate of electromagnetic information in space.

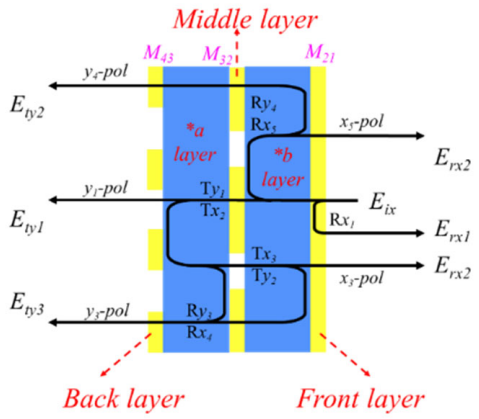

FIGURE 1. Fabry-Perot cavity model of unit structure.

In particular, the unit structure incorporates front and back grating layers that function as selectors for x and y polarizations, while the middle layer is employed as a generator for polarization conversion. The majority of incident x-polarized waves can pass through the upper grating, while the middle layer separates the incident waves into cross-polarized and co-polarized components. Subsequently, the y-polarized component is allowed to pass through the underlying y-polarized selective grating. However, the x-polarized component will be completely reflected and interact with the middle and top layers again. The resonance processes described above are repeated multiple times for both the cross-polarized and co-polarized components of the electromagnetic field. Eventually, the transmission amplitude of T_{xy} is close to "1", causing a high polarization conversion efficiency.

Apply the propagation matrix method to further analyze the unit working principle, namely the full space properties [25]. M_{ab} represents the correlation between the forward and reverse propagation fields when the electromagnetic wave is vertically incident on the unit structure.

$$M_{ab}\begin{bmatrix} E^f_{bx} \\ E^f_{by} \\ E^L_{bx} \\ E^L_{by} \end{bmatrix} = \begin{bmatrix} E^f_{ax} \\ E^f_{ay} \\ E^L_{ax} \\ E^L_{ay} \end{bmatrix} \tag{1}$$

where *am* and *bm* are the propagation of m (x or y) polarized electromagnetic waves in media a and b, respectively. E^L_{am} and E^L_{bm} represent the electric field of m polarized electromagnetic waves in media a and b, respectively. f and L denote the forward and reverse propagation directions. From the derivation, M_{ab} can be obtained as:

$$\begin{aligned} M_{ab} = & \begin{bmatrix} 1 & 0 & -r_{ax,ax} & -r_{ax,ay} \\ 0 & 1 & -r_{ay,ax} & -r_{ay,ay} \\ 0 & 0 & t_{bx,bx} & t_{bx,by} \\ 0 & 0 & t_{by,bx} & t_{by,by} \end{bmatrix}^{-1} \\ & \times \begin{bmatrix} t_{ax,bx} & t_{ax,by} & 0 & 0 \\ t_{ay,bx} & t_{ay,ax} & 0 & 0 \\ -r_{bx,bx} & -r_{bx,by} & 1 & 0 \\ -r_{by,bx} & -r_{by,by} & 0 & 1 \end{bmatrix} \end{aligned} \tag{2}$$

where r and t are the reflection and transmission amplitudes. When the refractive index of a uniform medium λ is ϕ_λ, the propagation matrix in the medium can be expressed as:

$$P_\lambda = \text{diag}\left(e^{ik\phi_x h}, e^{ik\phi_x h}, e^{-ik\phi_x h}, e^{-ik\phi_x h}\right) \tag{3}$$

Thus, the total propagation matrix M of the overall unit is defined as:

$$M = M_{43} \cdot P_\lambda \cdot M_{32} \cdot P_\lambda \cdot M_{21} \tag{4}$$

Two dielectric layers and three metal structures are responsible for governing the resonance and propagation of electromagnetic waves within a Fabry-Perot cavity. The incident wave is decomposed into four parts: R_x, R_y (co-polarized and cross-polarized components of reflection), and T_x, T_y (co-polarized and cross-polarized components of transmission). The x-polarized wave incident along the $+z$ direction undergoes multiple reflections and transmissions in the Fabry-Perot cavity unit and is ultimately converted into a y-polarized wave with high conversion efficiency and transmission coefficient (see Figure 1).

3. THE UNIT STRUCTURE DESIGN OF THREE-CHANNEL

According to the Fabry-Perot cavity principle, a multifunctional multi-frequency full-space unit is constructed that gener-

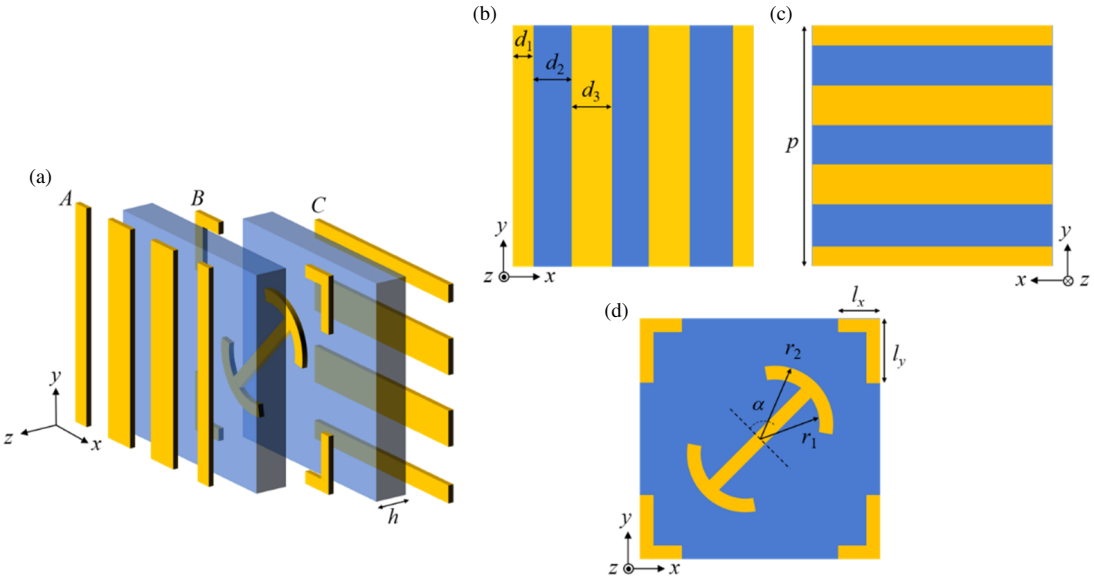

FIGURE 2. Unit structure diagram of Fabry-Perot cavity model: (a) Overall schematic diagram of the unit, (b) metal layer A, (c) metal layer B, (d) metal layer C.

ates high-performance reflected and transmitted waves simultaneously. The unit contains three layers of the metal structure, including gratings A and C on the upper and lower layers, as well as composite structure B with oblique open rings and a cross shape in the middle layer which are all made of "copper pure" (shown in Figure 2(a)). The thickness of the metal layers is 0.035 mm. Meanwhile, the metal layers are separated by two identical dielectric plates F4B$_{\mathrm{M}}$ ($\varepsilon_r = 3.5$, $\tan\delta = 0.001$), whose thickness is $h = 1$ mm. The periodicity of the unitary structure is $p = 4$ mm. By optimizing the parameters, the following fixed geometric parameters are obtained: $d_1 = 0.33$ mm, $d_2 = d_3 = 0.66$ mm, $r_1 = 1.6$ mm, $r_2 = 2$ mm. The transverse arm length l_x, the longitudinal arm length l_y of the cross-shaped structure, and the rotation angle α of the diagonal opening ring are set as variable parameters in metal layer B. $d \approx 2h = 2$ mm is the thickness of the cavity, and unit's resonant frequency is around 20 GHz.

From the unit structure design shown in Figure 2, it is apparent that the parameter changes of the oblique open loop and cross-shaped composite structure in the middle layer are used to implement the reflected and transmitted electromagnetic wave modulation at both ends of the unit structure. Establish a unit model in CST for simulation and optimization. Derived from the propagation principle, the geometrical parameters of the unit structure are optimized by discrete adjustment. The reflected phase at 31 GHz is obtained by adjusting the l_y under the y-polarized incident wave. For x-polarized incident waves, different reflected and transmitted phases at 32 GHz and 22 GHz can be reached by adapting l_x and α, respectively. Thereby, the lengths l_y are optimized to 1.4 mm and 2.49 mm, and the lengths l_x are evaluated to 1.8 mm and 2.4 mm.

Figures 3(a) and 3(b) illustrate the reflection amplitude and phase of the unit structure under y-polarized and x-polarized incidence waves, respectively. For the four coding units "U-0-0", "U-0-1", "U-1-0", and "U-1-1", the second and third digits act as the coding sequence of the unit under the incidence of x/y-LP, respectively. At a frequency of 31 GHz, when the y-LP is vertically incident along the $+z$ axis, and the remaining parameters are modified, the reflected amplitude exceeds 0.9, while the phase difference between "0" and "1" units is approximately 180° (as depicted in Figure 3(a)). That is to say, the amplitude and phase response under y-LP are only determined by l_y, and the changes in other parameters hardly affect them. The reflection amplitude and phase of the unit structure at 32 GHz under x-LP along $-z$ incidence are plotted in Figure 3(b). By adjusting the l_x parameter, units "0" and "1" achieve a phase difference of 180° with a reflection amplitude greater than 0.9, and the impact of other parameter changes is relatively small.

At 22 GHz, the rotation angle α of the unit is adapted to implement both "0-M-N" and "1-M-N" units under x-LP along $-z$ incidence. Figure 3(c) shows that in the frequency range, the transmission amplitude of the units is higher than 0.9, resulting in an efficient transmission performance. It should be noted that, regardless of changes made to other structural parameters, the phase difference between two units always remains at 180°. The analysis reveals that the unit exhibits a relatively high transmission amplitude and a flat phase-change curve, which contributes to the array's excellent beam modulation. The metasurface polarization conversion rate is defined as: PCR $= t_{yx}^2$; the polarization azimuth is defined as: $\theta = \mathrm{atan}(t_{yx}/t_{xx})$, where t_{yx} is the cross-polarization transmission amplitude, and t_{xx} is the co-polarization transmission amplitude. The polarization conversion ratio (PCR) is greater than 0.99 in the band range of 22 GHz, as depicted in Figure 3(d). Moreover, the polarization conversion azimuth of nearly 90° is equipped with the unit. According to the simulation results, nearly all x-polarized waves are converted into y-polarized waves, thereby denoting the achievement of an effective transmission polarization conversion capability.

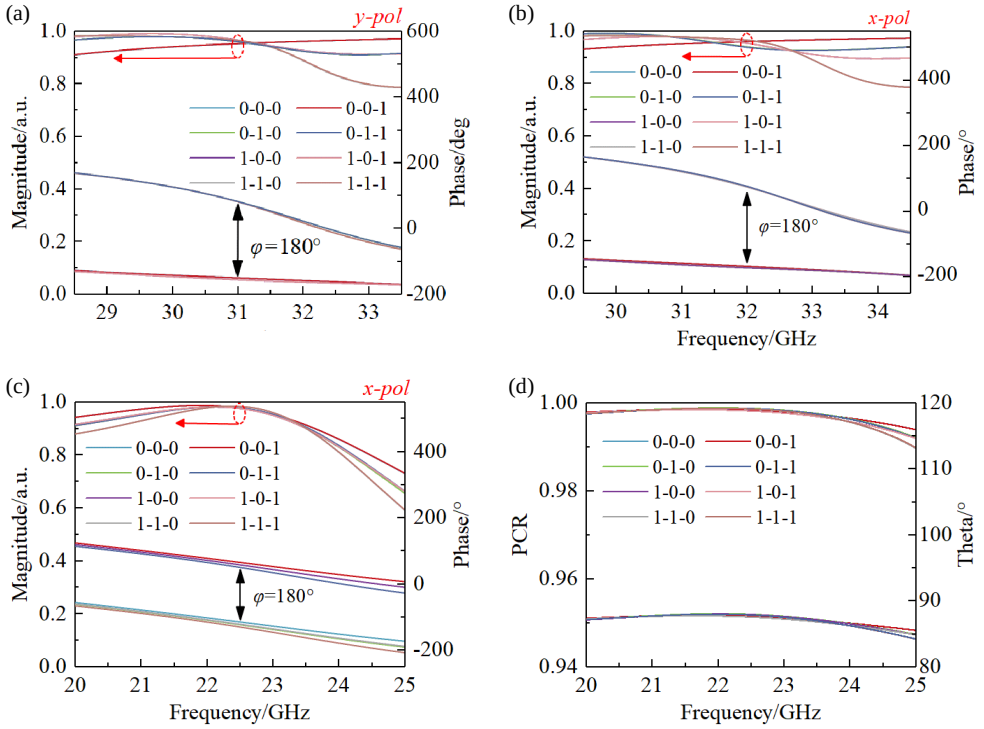

FIGURE 3. Full-space three-channel unit simulation results: (a) Reflection amplitude and phase response results at 31 GHz, (b) reflection amplitude and phase response results at 32 GHz, (c) transmission amplitude and phase response results at 22 GHz, (d) polarization conversion coefficient and azimuth results at 22 GHz.

Hence, independent phase control of different polarizations, frequency bands, and incident directions, as well as high reflection and transmission performance, can be realized by varying the unit structure parameters l_y, l_x, and α. The specific parameters are displayed in Table 1.

TABLE 1. Coding sequence, size, and rotation angle of units.

Frequency	31 GHz	32 GHz	22 GHz
Code method	l_y/mm	l_x/mm	α/°
0-0-0	1.4	1.8	0
0-0-1	2.49	1.8	0
0-1-0	1.4	2.4	0
0-1-1	2.49	2.4	0
1-0-0	1.4	1.8	90
1-0-1	2.49	1.8	90
1-1-0	1.4	2.4	90
1-1-1	2.49	2.4	90

The surface current of the multi-channel unit was simulated (see Figure 4) to further discuss the issue of crosstalk between distinct channels and to demonstrate that an independent electromagnetic wave phase response may be obtained on the same aperture. When the y-LP is incident along the $+z$ axis (shown in Figure 4(a)), strong current occurs mainly in the longitudinal arm length of the cross structure, which indicates that the structure resonates at 31 GHz. At 32 GHz, x-LP is incident along the $-z$ axis (shown in Figure 4(b)), strong current appears in the transverse arm length of the cross structure. So, the transverse and longitudinal arms of the cross structure only resonate with the incident wave parallel to the arm direction and have good isolation. Similarly, when a 22 GHz x-LP is incident along the $-z$ axis (shown in Figure 4(c)), there is a small amount of current on the cross structure, but the current density is more concentrated on the oblique open loop. In summary, the oblique open-loop structure resonates in the low-frequency band but barely works in the reflected band, as observed from the surface currents.

The above results further prove that there is a lower frequency band crosstalk between the cross-shaped structure and oblique open-loop structure. To summarize, the unit structure that has been designed exhibits the capability to achieve spatial, frequency band, and polarization reuse effectively. This characteristic proves highly beneficial in enabling the realization of multi-channel, multifunctional, and full space integration of metasurface arrays on a single structure.

4. THE DESIGN OF A THREE-CHANNEL MULTIFUNCTIONAL METASURFACE

Figure 5 presents a conceptual diagram of the proposed metasurface, which allows multi-channel multi-frequency multiplexing in both reflection and transmission modes. The three functions of beam deflection (f_1), RCS reduction (f_2), and focusing (f_3) within the same metasurface array aperture are accomplished by judiciously formulating the phase-coding sequence under diverse frequency bands, incident directions, and

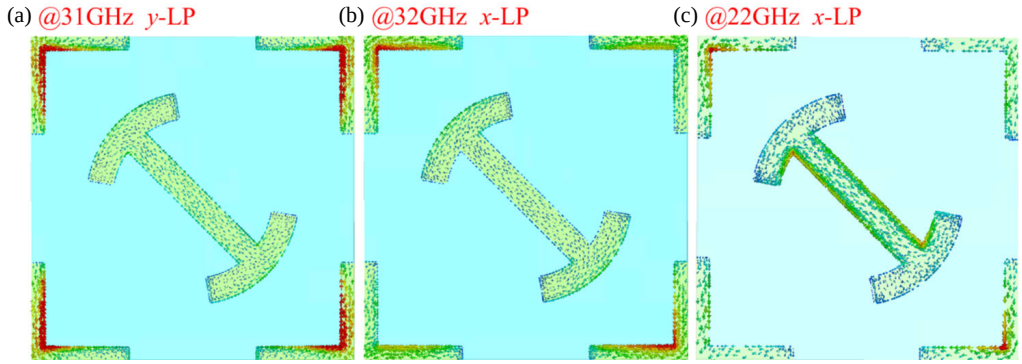

FIGURE 4. Diagram of simulation results of metal surface current in layer B of unit: (a) 31 GHz, (b) 32 GHz, (c) 22 GHz.

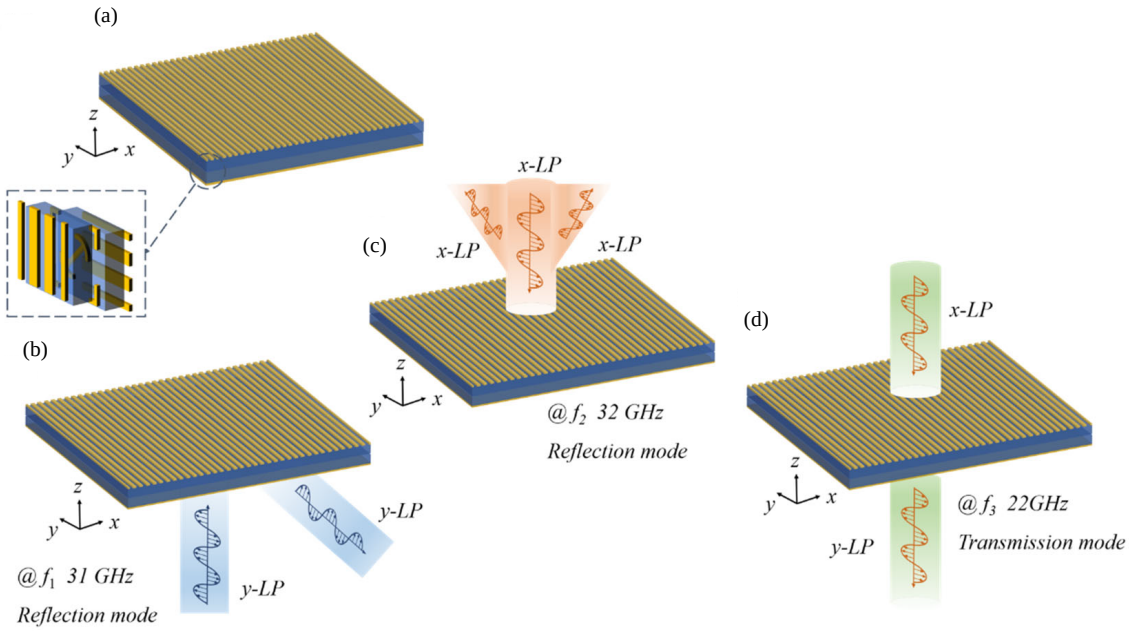

FIGURE 5. Three-channel multi-function multi-band multiplexed coding metasurface diagram: (a) Metasurface structure, (b) reflection function f_1, (c) reflection function f_2, (d) transmission function f_3.

polarizations. The metasurface array contains 32×32 unit structures with a total size of 128 mm $\times$ 128 mm $\times$ 2.105 mm.

The first function (f_1) beam deflection of the metasurface is implemented in the $-z$ direction half-space. The y-LP vertically incident electromagnetic wave at 31 GHz is directionally reflected to a specific angle of 17° with respect to the $-z$ axis. The total electric field energy in the $-z$ direction half-space of the metasurface can be attained by superimposing the electric fields of its reflected beams, ultimately achieving the function of beam deflection. Taking a point in the center direction of the mth beam as f_m, the phase distribution of the superimposed electric field required to form the reflected beam can be expressed as:

$$\varphi_E(x,y) = \arg \sum_{m=1}^{M} \left[F_m \exp(-jk \left| \overrightarrow{f_m} \right|) \right] \tag{5}$$

where F_m denotes the amplitude in the direction of the center of the mth reflected beam, and k is the wave vector. When the electromagnetic wave from the feed is normally incident on the metasurface array, the phase distribution of the radiated electric field is φ_k. Thus, the total phase distribution required for the reflected beam-splitting metasurface is defined as:

$$\varphi(x_{ij}, y_{ij}) = \mathrm{mod}\left[\varphi_E(x_i, y_i) - \varphi_k(x_i, y_i), 2\pi\right] \tag{6}$$

The sequence of the metasurface function (f_1) can be calculated employing the electric field superposition theorem. By changing the numerical magnitude of F_m and distance d, the target beam is set to a single beam and off-axis. Figure 6(a) displays the size distribution of the metasurface as calculated. Figures 6(b) and 6(c) describe the simulated results of the two-dimensional and three-dimensional far-field scattering plots of the metasurface under the illumination of the y-LP incident wave. It is clear that the main flap of the reflected wave is noticeably deviated from the $-z$ axis by 17°. To further verify the beam deflection characteristics of the metasurface, the electric field distribution at 31 GHz was simulated. The energy of the reflected electric field is mainly concentrated on the right-hand

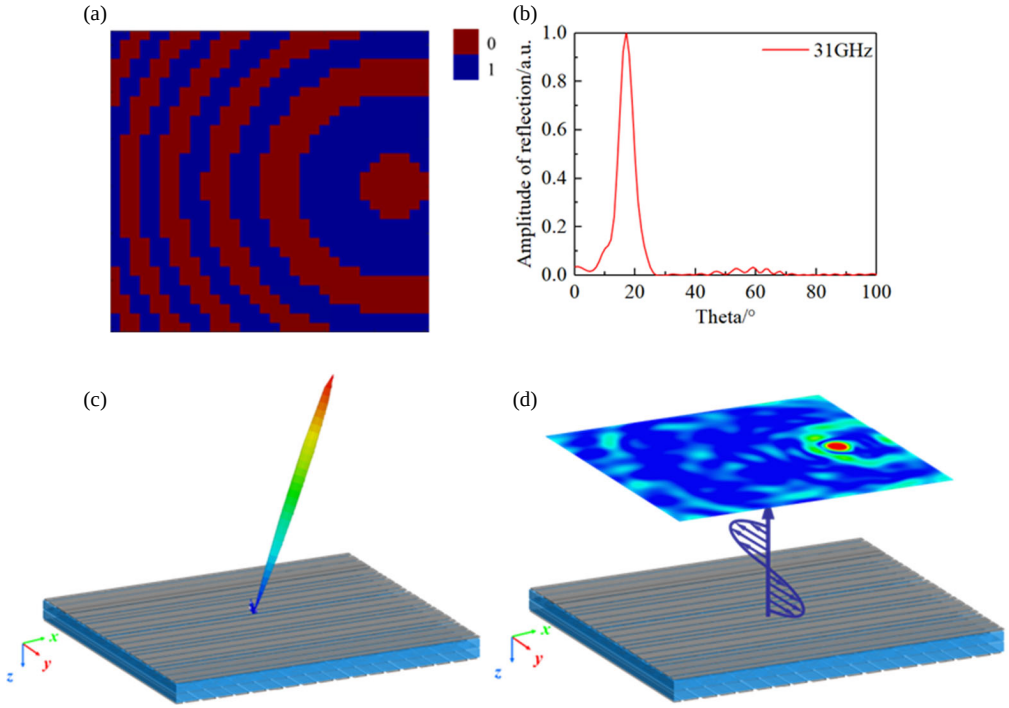

FIGURE 6. Study on the performance of y-LP incident metasurface at 31 GHz: (a) Metasurface size distribution, (b) two-dimensional results, (c) three-dimensional results, (d) electric field distribution of metasurface on *xoy* plane.

region, while the energy of other sidelobes is lower (see Figure 6(d)).

When a 32 GHz x-LP wave is incident along the $-z$ direction, the achievement of the second function RCS reduction (f_2) of the full-space metasurface is observed. The ideal value of the array sequence is solved using the particle population optimization algorithm, which is derived from the far field scattering theorem of metasurfaces (Equation (7)):

$$f(\theta,\psi) = f_e(\theta,\psi)\sum_{m=1}^{N}\sum_{n=1}^{N}\exp\{-i\{\psi(m,n) + KD(m-1/2)\sin\theta\cos\psi + KD(n-1/2)\sin\theta\sin\psi\}\} \quad (7)$$

where θ and ψ are the pitch and azimuth angles of the reflected beam; $\psi(m,n)$ is the reflected phase response of a single unit to an incident electromagnetic wave; m and n are the coordinate values of the unit. D is the period length of the metasurface, and K is the propagation vector. Figure 7(a) presents the encoding sequence of function (f_2). The metasurface array is modeled in CST using the optimized encoding sequence as the foundation. Figure 7(d) depicts this array's three-dimensional far-field scattering pattern. Electromagnetic waves are reflected by the array and form countless randomly oriented electromagnetic wave beams in the upper half of space, known as diffuse scattering beams. To further demonstrate the RCS reduction performance of the array, we draw 3D far-field scattering for the same incidence case and the same size of metal plate (displayed in Figure 7(c)). The reflected electromagnetic wave energy in the normal direction is effectively suppressed. Concurrently, quantitative numerical analysis was carried out (displayed in Figure 7(b)), and a -14 dB RCS decrease was attained by the encoded metasurface in the *xoy* plane ($\varphi = 0°$) compared to the metal plate.

For function (f_3), the transmitted wave focuses in the lower half space of the metasurface under the illumination of x-LP waves at 22 GHz toward $-z$ directions and achieves polarization conversion. The electric field distribution on the metasurface comes from the wavefront superposition of the focused target field. Hence, given the wavefront information of the focused target field, the phase distribution of the metasurface can be obtained. The radiation field distribution E of a single focal point can be obtained after discretizing the target field. The compensation phase φ required for the array can be obtained by overlaying the electric field generated by multiple focal points. Due to the reversibility of light, the reconstructed electric field will reverse to form multiple focal points, ultimately resulting in the desired focused target field.

$$E = \sum_{n=1}^{N}\left[\frac{w_n(x_i,y_i,0)\cdot\exp(jkR_n)}{R_n}\right] \quad (8)$$

$$\varphi(x_i,y_i,0) = \varphi_r - \text{angle}\,E(x_i,y_i,0) \quad (9)$$

where w_n is the intensity factor of the nth discrete focus, R_n the distance from the nth discrete focus to the ith unit of the metasurface, k the wave vector, and φ_r the compensation phase from the feed source to the metasurface.

The transmission focusing plane of the full-space frequency multiplexed metasurface at 100 mm forms an "I"-liked focusing pattern, and the required phase distribution is shown in Figure 8(a). The CST simulation result (Figure 8(b)) displays the

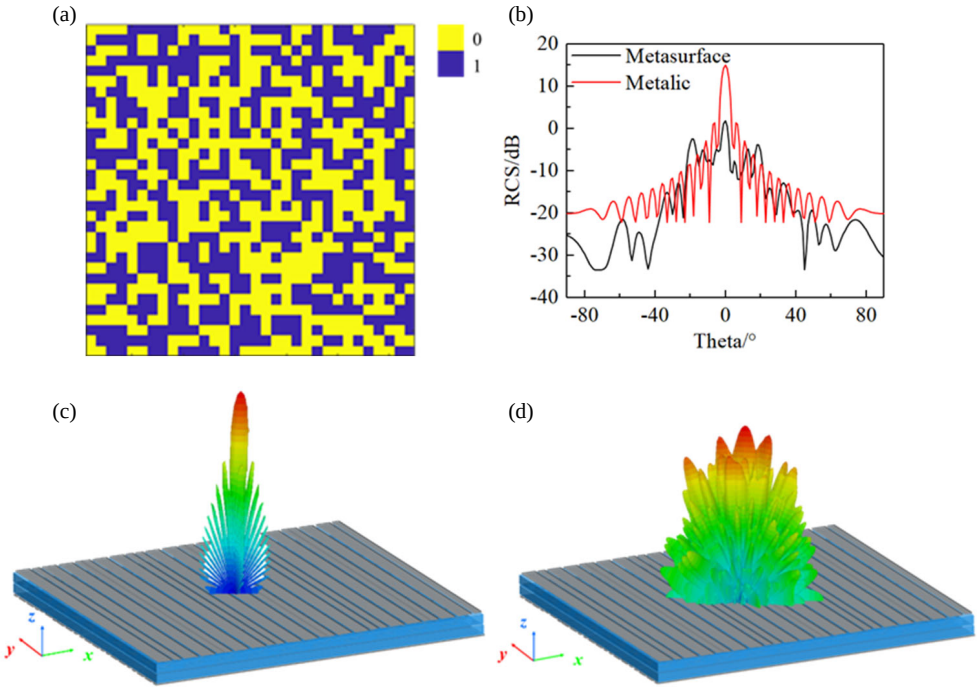

FIGURE 7. Study on the performance of x-LP incident metasurface at 32 GHz: (a) Metasurface size distribution, (b) two-dimensional results of coded metasurface and the metal reference plate of same size, (c) three-dimensional results of metal reference plate of the same size, (d) three-dimensional results of coded metasurface.

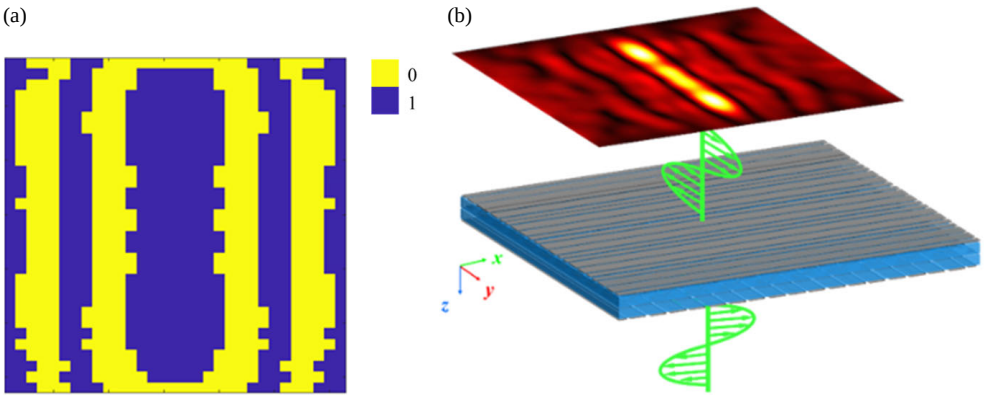

FIGURE 8. Study on the properties of x-LP incident metasurface at 22 GHz: (a) Phase distribution of metasurfaces, (b) electric field distribution of metasurface on the *xoy* plane.

distribution of cross-polarized electric field intensity scanned on a focusing plane at a fixed distance from the metasurface. Obviously, the cross-polarized transmitted wave has strong electric field spots on the "I" line of the target focusing plane, and the electric field distribution is uniform. The ratio of the incident wave energy to the focusing energy of the "I" image is defined as the focusing efficiency, which can be calculated to be 38.75%.

For the above simulation results, the versatility of beam deflection, RCS reduction, and focusing were easily fulfilled by the proposed full-space metasurface design scheme. The total size distribution of the metasurface B-layer metal, which contains eight coding unit structures, can be obtained by the above coded sequence calculation analysis, as shown in Figure 9(a). The metasurface has reflected phase responses at 31 GHz and 32 GHz, respectively, while it has a transmitted phase response at 22 GHz. The simulation results illustrate that the proposed metasurface permits the easy realization of diverse electromagnetic wave modulation in full-space on a single aperture, as exemplified by beam deflection (Figure 9(b)), RCS reduction (Figure 9(c)), and focusing (Figure 9(d)).

As shown in Table 2, a comparison of the work in this paper with other recent publications is presented. In [26], the metasurfaces can achieve dual-band, four-channel multifunctionality, but only the electromagnetic information in the upper half space of the metasurface is utilized. Although full-space electromagnetic wave control is implemented in [27], it only operates in one frequency band. Compared to [28], the proposed full space design scheme in this paper has smaller unit cycles, thickness, and size, which is more conducive to integra-

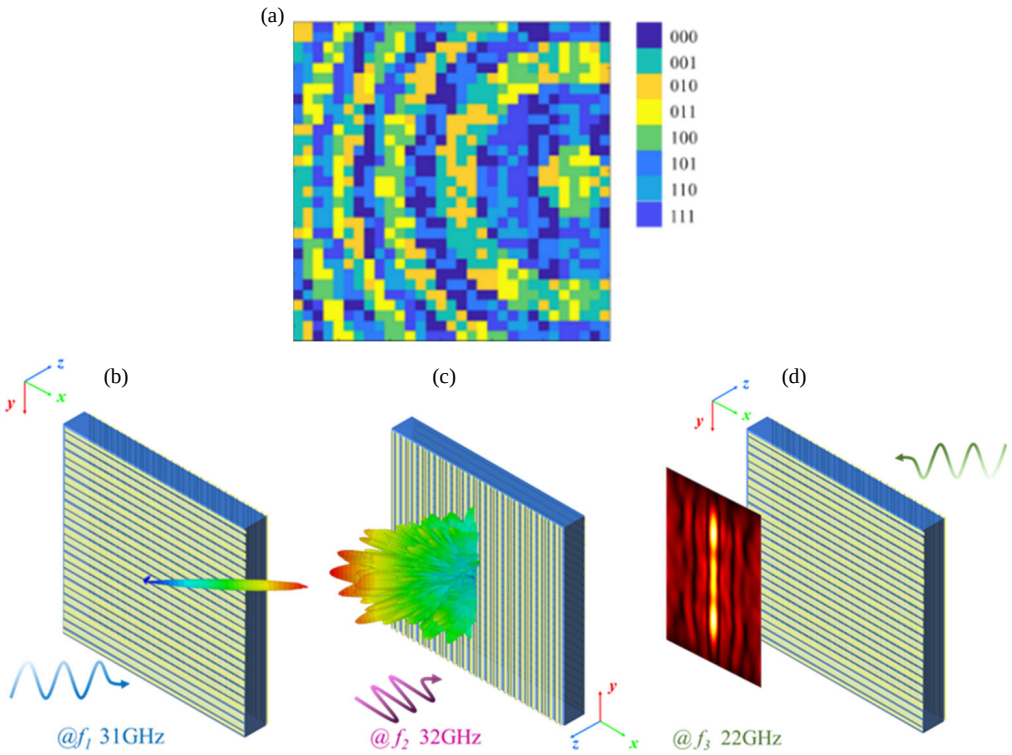

FIGURE 9. Coded metasurface multifunctional simulation results: (a) Unit size distribution of layer B, (b) reflection function at 31 GHz, (c) reflection function at 32 GHz, (d) transmission function at 22 GHz.

TABLE 2. Comparison of references.

references	frequency	size	space	channel number
[26]	8/15 GHz	352 mm × 352 mm	half-space	4
[27]	15 GHz	240 mm × 240 mm	full-space	2
[28]	7.7/8.4/9/15/15.9/16.5 GHz	375 mm × 375 mm × 17.172 mm	full-space	6
this work	22/31/32 GHz	128 mm × 128 mm × 2.105 mm	full-space	3

tion. Simultaneously, the three-channel multi-frequency multiplexing full-space metasurface proposed in this article greatly expands the electromagnetic information capacity of metasurfaces from an informatics perspective and enriches the control space of electromagnetic waves.

5. CONCLUSIONS

In conclusion, a multi-layer unit structure has been presented in this research that can control reflected and transmitted waves by changing the direction, frequency ranges, and polarization of the incident waves, and can avoid crosstalk between channels. By elaborately combining the unit structure with a specific coding sequence, three independent electromagnetic wave control functions can be achieved. The simulation results meet the expected theoretical calculation results, indicating that the x-polarized wave incident along the $-z$ direction at 22 GHz achieves polarization conversion and focusing functions of the transmitted wave. Meanwhile, the abnormal deflection and RCS reduction of the reflected beam are implemented under the excitation of y-polarized wave incident along the $+z$ direction at 31 GHz and x-polarized wave incident along the $-z$ direction at 32 GHz, respectively.

This paper achieves multiplexing of electromagnetic waves in frequency, polarization, and space, greatly improving the utilization of electromagnetic information. However, due to time and experimental conditions limitations, no research has been conducted on the multiplexing of electromagnetic waves in other dimensions such as amplitude and circular polarization mode. Further exploration is needed for multifunctional integrated metasurfaces. In addition, 3-bit phase discretization on the three variable parameters of the metasurface is conducted, which reduces the complexity of the design while limiting the accuracy of the implementation effect. Even so, the proposed full-space frequency multiplexing unit structure is simple and efficient, and its combination with different functional coding sequences has potential application value in highly integrated communication equipment and electromagnetic systems. Furthermore, it can also be easily applied to other bands, such as

terahertz and optical bands, and can be extended to other multifunctional devices, like radomes and multiplexers.

ACKNOWLEDGEMENT

This work was supported by the [Chongqing Natural Science Foundation General Program] under Grant [number CSTB2022NSCQ-MSX0960].

REFERENCES

[1] Tian, S., X. Zhang, X. Wang, J. Han, and L. Li, "Recent advances in metamaterials for simultaneous wireless information and power transmission," *Nanophotonics*, Vol. 11, No. 9, 1697–1723, 2022.

[2] Iyer, A. K., A. Alu, and A. Epstein, "Metamaterials and metasurfaces — Historical context, recent advances, and future directions," *IEEE Transactions on Antennas and Propagation*, Vol. 68, No. 3, 1223–1231, 2020.

[3] Li, W., B. Zhang, Y. Ying, J. Yu, J. Zheng, L. Qiao, J. Li, and S. Che, "An optically transparent unequal proportional coding metasurface with absorption and diffusion integrated mechanism for ultra-broadband RCS reduction," *Optical Materials*, Vol. 133, 112801, 2022.

[4] Mu, Y., M. Zheng, J. Qi, H. Li, and J. Qiu, "A large field-of-view metasurface for complex-amplitude hologram breaking numerical aperture limitation," *Nanophotonics*, Vol. 9, No. 16, 4749–4759, 2020.

[5] Tutar, F. and G. Ozturk, "An effective metasurface-based linear and circular polarization converter for C- and X-band applications," *Optical Materials*, Vol. 128, 112355, 2022.

[6] Li, X. M., X. Xi, J. Chen, H. B. Wu, X. Li, Q. Chen, and R.-X. Wu, "Stereo meta-atom enabled phase-amplitude gradient metasurface for circularly polarized waves," *Advanced Optical Materials*, Vol. 10, No. 13, 2200326, 2022.

[7] Bai, G. D., Q. Ma, S. Iqbal, L. Bao, H. B. Jing, L. Zhang, H. T. Wu, R. Y. Wu, H. C. Zhang, C. Yang, and T. J. Cui, "Multitasking shared aperture enabled with multiband digital coding metasurface," *Advanced Optical Materials*, Vol. 6, No. 21, 1800657, 2018.

[8] Xie, R., M. Xin, S. Chen, D. Zhang, X. Wang, G. Zhai, J. Gao, S. An, B. Zheng, H. Zhang, and J. Ding, "Frequency-multiplexed complex-amplitude meta-devices based on bispectral 2-bit coding meta-atoms," *Advanced Optical Materials*, Vol. 8, No. 24, 2000919, 2020.

[9] Zhang, Q., R. Xie, Z. Gu, H. Zhang, C. Chen, J. Ding, and W. Chen, "Broadband high-efficiency polarization-encoded meta-holograms based on 3-bit spin-decoupled reflective meta-atoms," *Optics Express*, Vol. 30, No. 3, 4249–4260, 2022.

[10] Li, J., Y. Cheng, and X. Li, "Terahertz transmission-type metasurface for the linear and circular polarization wavefront manipulation," *Advanced Theory and Simulations*, Vol. 5, No. 8, 2200151, 2022.

[11] Fu, C., L. Han, C. Liu, X. Lu, and Z. Sun, "Combining Pancharatnam-Berry phase and conformal coding metasurface for dual-band RCS reduction," *IEEE Transactions on Antennas and Propagation*, Vol. 70, No. 3, 2352–2357, 2022.

[12] Ali, L., Q. Li, T. A. Khan, J. Yi, and X. Chen, "Wideband RCS reduction using coding diffusion metasurface," *Materials*, Vol. 12, No. 17, 2708, 2019.

[13] Lai, P., Z. Li, W. Wang, J. Qu, L. Wu, T. Lv, B. Lv, Z. Zhu, Y. Li, C. Guan, H. Ma, and J. Shi, "Transmissive 2-bit anisotropic coding metasurface," *Chinese Physics B*, Vol. 31, No. 9, 098102, 2022.

[14] Zhang, D., X. Cao, H. Yang, J. Gao, and X. Zhu, "Multiple OAM vortex beams generation using 1-bit metasurface," *Optics Express*, Vol. 26, No. 19, 24 804–24 815, 2018.

[15] Esmail, B. A. F., M. K. A. Rahim, H. A. Majid, N. A. Murad, N. A. Samsuri, O. Ayop, A. Salh, and N. Al-Fadhali, "Deflected beam pattern through reconfigurable metamaterial structure at 3.5 GHz for 5G applications," *Waves in Random and Complex Media*, 1–24, 2022.

[16] Li, X., J. Chen, X. Xi, X. Li, Q. Cheng, and R.-X. Wu, "Broadband trifunctional metasurface and its application in a lens antenna," *Optics Express*, Vol. 29, No. 15, 23 244–23 257, 2021.

[17] Yuan, Y., K. Zhang, B. Ratni, Q. Song, X. Ding, Q. Wu, S. N. Burokur, and P. Genevet, "Independent phase modulation for quadruplex polarization channels enabled by chirality-assisted geometric-phase metasurfaces," *Nature Communications*, Vol. 11, No. 1, 4186, 2020.

[18] Xu, H.-X., C. Wang, G. Hu, Y. Wang, S. Tang, Y. Huang, X. Ling, W. Huang, and C.-W. Qiu, "Spin-encoded wavelength-direction multitasking janus metasurfaces," *Advanced Optical Materials*, Vol. 9, No. 11, 2100190, 2021.

[19] Yang, L.-J., S. Sun, W. E. I. Sha, and J. Hu, "Bifunctional integration performed by a broadband high-efficiency spin-decoupled metasurface," *Advanced Optical Materials*, Vol. 11, No. 2, 2201955, 2023.

[20] Zheng, B., H. Ren, S. An, H. Tang, H. Li, M. Haerinia, Y. Dong, C. Fowler, and H. Zhang, "Tunable metasurface with dynamic amplitude and phase control," *IEEE Access*, Vol. 9, 104 522–104 529, 2021.

[21] Cui, T. J., S. Liu, G. D. Bai, and Q. Ma, "Direct transmission of digital message via programmable coding metasurface," *Research*, Vol. 2019, 2584509, 2019.

[22] Dong, L., T. C. Li, L. Zhu, X. Zhao, and J. Yi, "Frequency-polarization-multiplexed single-layer coding metasurface for independent control of four-channel wavefront," *Annalen Der Physik*, Vol. 533, No. 12, 2100300, 2021.

[23] Li, Z. Y., S. J. Li, B. W. Han, G. S. Huang, Z. X. Guo, and X. Y. Cao, "Quad-band transmissive metasurface with linear to dual-circular polarization conversion simultaneously," *Advanced Theory and Simulations*, Vol. 4, No. 8, 2100117, 2021.

[24] Shang, G., G. Hu, C. Guan, Y. Wang, K. Zhang, Q. Wu, J. Liu, X.-M. Ding, S. N. Burokur, H. Li, X. Ding, and C.-W. Qiu, "A non-interleaved bidirectional janus metasurface with full-space scattering channels," *Nanophotonics*, Vol. 11, No. 16, 3729–3739, 2022.

[25] Shang, G., C. Guan, K. Zhang, Q. Wu, J. Liu, X. Ding, H. Li, S. N. Burokur, and X. Ding, "Design of a frequency-multiplexed metasurface with asymmetric transmission," *Optics Letters*, Vol. 47, No. 17, 4504–4507, 2022.

[26] Luo, X.-Y., W.-L. Guo, K. Qu, Q. Hu, K. Chen, H. Tang, J. Zhao, T. Jiang, and Y. Feng, "Quad-channel independent wavefront encoding with dual-band multitasking metasurface," *Optics Express*, Vol. 29, No. 10, 15 678–15 688, 2021.

[27] Dong, L., X. S. Li, L. Zhu, S. N. Burokur, Q. Wu, and X. M. Ding, "Full-space double-layer patterned 2-bit coding metasurface hologram," *Annalen Der Physik*, Vol. 534, No. 10, 2200229, 2022.

[28] Wu, L. W., H. F. Ma, Y. Gou, R. Y. Wu, Z. X. Wang, Q. Xiao, and T. J. Cui, "Multitask bidirectional digital coding metasurface for independent controls of multiband and full-space electromagnetic waves," *Nanophotonics*, Vol. 11, No. 12, 2977–2987, 2022.